EES Catalysis

PAPER

View Article Online
View Journal | View Issue

Cite this: *EES Catal.*, 2025, 3, 106

Computer-aided design of Pt/In_2O_3 single-atom catalysts for CO_2 hydrogenation to methanol†

Yuchen Wang,‡[abc] Zixuan Zhou,‡[ab] Bin Qin,‡[a] Qingyu Chang,‡[a] Shanshan Dang,[a] Yiqin Hu,[d] Kun Li,[c] Yuanjie Bao,[ab] Jianing Mao,[be] Haiyan Yang,[a] Yang Liu,[c] Jiong Li,[e] Shenggang Li,*[abcf] David A. Dixon,*[d] Yuhan Sun[acg] and Peng Gao*[abf]

Received 8th October 2024,
Accepted 3rd November 2024

DOI: 10.1039/d4ey00218k

rsc.li/eescatalysis

Methanol (CH_3OH) synthesis from carbon dioxide (CO_2) hydrogenation is an industrially viable approach to CO_2 utilization. For the recently developed indium oxide (In_2O_3) catalyst, higher performance may be achieved by introducing transition metal promoters, although recent studies suggest that single atom sites favour CO formation. Here, by density functional theory-based microkinetic simulations, bulk-doped Pt/In_2O_3 single atom catalysts (SACs) with much higher CO_2 reactivity than the In_2O_3 catalyst while maintaining CH_3OH selectivity were designed. Several Pt/In_2O_3 SACs were synthesized to confirm our theoretical predictions. The synthesized Pt/In_2O_3 SAC in the predominantly bulk-doped form exhibits much higher CO_2 reactivity than the In_2O_3 catalyst with high stability and similar CH_3OH selectivity, yielding a CH_3OH productivity of 1.25 g g_{cat}^{-1} h^{-1}. This study demonstrates the power of computational methods in designing oxide-based catalysts for industrial reactions and reveals a bulk-doped SAC with high performance.

Broader context

Rapid increase in the amount of CO_2 emission from fossil fuel consumption accelerates the approaching of climate change, and efficient and sustainable technologies must be swiftly developed and widely deployed to mitigate such severe consequence. Central to CO_2 capture and utilization for reducing CO_2 emission, CO_2 hydrogenation to valuable chemicals such as methanol using renewable hydrogen is economically and technologically viable for applications at industrial scale. However, presently known catalysts for methanol synthesis from CO_2 hydrogenation have suboptimal catalytic performance due to poor activity, low stability, or limited selectivity. For rapid development of more efficient catalysts for this important reaction, first principles-based simulations were employed to rationally design a Pt/In_2O_3 single atom catalyst in the unusual bulk-doped form, which was shown by our experiments to enable unprecedented methanol productivity of 1.25 g g_{cat}^{-1} h^{-1} under reaction conditions of 5.0 MPa, 573 K and 54 000 mL g_{cat}^{-1} h^{-1}, far exceeding the current reported maximum methanol productivity of less than 1.0 g g_{cat}^{-1} h^{-1}.

[a] *CAS Key Laboratory of Low-Carbon Conversion Science and Engineering, Shanghai Advanced Research Institute, Chinese Academy of Sciences, Shanghai 201210, China. E-mail: lisg@sari.ac.cn, gaopeng@sari.ac.cn*
[b] *University of Chinese Academy of Sciences, Beijing 100049, China*
[c] *School of Physical Science and Technology, ShanghaiTech University, Shanghai 201210, China*
[d] *Department of Chemistry and Biochemistry, The University of Alabama, Shelby Hall, Box 870336, Tuscaloosa, Alabama 35487-0336, USA. E-mail: dadixon@ua.edu*
[e] *Shanghai Synchrotron Radiation Facility, Shanghai Advanced Research Institute, Chinese Academy of Sciences, Shanghai 201204, China*
[f] *State Key Laboratory of Low Carbon Catalysis and Carbon Dioxide Utilization, Shanghai Advanced Research Institute, Chinese Academy of Sciences, Shanghai 201210, China*
[g] *Shanxi Research Institute, Huairou Research Laboratory, Taiyuan 030032, China*

† Electronic supplementary information (ESI) available. See DOI: https://doi.org/10.1039/d4ey00218k

‡ These authors contributed equally: Yuchen Wang, Zixuan Zhou, Qingyu Chang and Bin Qin.

Introduction

Global warming and climate change induced by the excessive combustion of fossil fuels leading to growing carbon dioxide (CO_2) emissions from the chemical and energy industries endanger the sustainable development of our society, so effective means for their mitigation must be sought. CO_2 capture and utilization (CCU) is widely recognized as a viable approach for reducing emissions while providing carbon-based chemicals and fuels that are widely used in our society. With renewable hydrogen, CO_2 hydrogenation over heterogeneous catalysts allows for sustainable production of fuels and chemicals including methanol (CH_3OH) with the key advantages of potential large-scale industrial applications using existing technologies and facilities.[1,2]

Cu-based catalysts are the most widely studied catalysts for methanol synthesis from syngas (carbon monoxide and dihydrogen, CO and H_2) and also from CO_2 hydrogenation, but poor catalyst stability and CH_3OH selectivity limit the latter applications.[3–10] In the past decade, a promising family of oxide-based catalysts, such as indium oxide (In_2O_3), which exhibit great catalyst stability, high catalytic activity, and excellent CH_3OH selectivity, especially when supported by an oxide support, such as zirconium oxide or optimized for the crystalline phase and exposed facets, has emerged.[11–14] Nevertheless, there is significant interest in further improving the CO_2 reactivity of In_2O_3-based catalysts, for example, *via* transition metal promotion,[15,16] in which CO formation *via* the reverse water gas shift (RWGS) reaction must be inhibited to maintain CH_3OH selectivity.

Compared with metal nanoparticles modified In_2O_3, metal-promoted In_2O_3 (M/In_2O_3) catalysts with highly dispersed metal sites were found more effective for CO_2 hydrogenation to methanol.[17–20] M/In_2O_3 in the form of single atom catalysts (SACs) has significant advantages such as high metal utilization and large cost reduction, especially for noble metals. However, there are few studies of CO_2 hydrogenation to methanol on M/In_2O_3 SACs.[16,21,22] Although good CO_2 reactivity and CH_3OH selectivity have been reported for Rh/In_2O_3 SACs,[16] a recent theoretical study[23] suggests that introducing atomic metal promoters such as Ni in the form of a surface dopant or an adatom can be detrimental to CH_3OH selectivity and may lead predominantly to CO formation. This casts doubt on the effectiveness of M/In_2O_3 SACs in promoting the methanol synthesis reaction and raises questions regarding the nature of the metal-induced promotional effect in these catalysts, which significantly limits targeted catalyst design.

Most SACs reported in the literature involve active atomic metal sites over the support surface, where the supports are mostly inactive,[24–26] whereas atomic metal promoters present in the bulk of the supports are assumed to have no significant reactivity. However, the M/In_2O_3 SACs for CO_2 hydrogenation are quite unique in that the In_2O_3 support is catalytically active, and the complex interaction between metal sites and In_2O_3 can significantly affect catalytic behaviours, so it is a great challenge to design and synthesize highly efficient M/In_2O_3 SACs for methanol synthesis.

In this work, we performed density functional theory (DFT) calculations and microkinetic simulations to elucidate the role of a platinum (Pt) dopant in Pt/In_2O_3 SACs for CO_2 hydrogenation. Our simulations show that surface atomic Pt sites are detrimental to CH_3OH formation, while surprisingly, the presence of bulk atomic Pt dopants greatly enhances CO_2 reactivity while maintaining CH_3OH selectivity. Our theoretical predictions are confirmed by the synthesis, evaluation, and characterization of several Pt/In_2O_3 SACs prepared using different methods. This study demonstrates the computer-aided design and experimental realization of highly efficient Pt/In_2O_3 SACs, and showcases the bulk-doped form of SACs with high performance.

Experimental

Density functional theory calculations

Spin-polarized DFT calculations were performed with the Vienna ab initio simulation package (VASP)[27–30] using the Bayesian error estimation functional with van der Waals correlation (BEEF-vdW)[31] and the projector-augmented wave (PAW) method.[32,33] Transition states were optimized using the climbing-image nudged elastic band (CI-NEB)[34] and dimer[35] methods as implemented in the transition state tools for VASP (VTST), and were further verified by numerical frequency calculations. Charge density difference analysis was performed using the VESTA program,[36] whereas all structures were built and visualized using Materials Visualizer from Materials Studio.

The $In_2O_3(111)$ surface was modelled with a stoichiometric and symmetric $p(1 \times 1)$ slab consisting of 72O and 48In atoms distributed in three O–In–O trilayers, where the bottom trilayer was fixed at its bulk position and a vacuum layer of 15 Å was inserted between adjacent slabs. A Γ-centred Monkhorst–Pack *k*-point mesh of $(3 \times 3 \times 1)$, an energy cutoff of 400 eV, and a force convergence of 0.03 eV $Å^{-1}$ were applied in the DFT calculations, similar to our previous works on this system[12,37–41]

Two types of SAC models for Pt/In_2O_3 were built by substituting one of the surface and bulk In atoms in the above $In_2O_3(111)$ slab model. The most probable $Pt/In_2O_3(111)$ structure in each case was determined by predicting the energetically most favourable location for the substitution, whose thermal stability was further verified by calculating the adhesive energy (ΔE_{adh}) of the Pt single atom from eqn (1)

$$\Delta E_{adh} = E_{Pt/In_2O_3(111)} - E_{Pt} - E_{V_{In}/In_2O_3(111)} \quad (1)$$

where $E_{Pt/In_2O_3(111)}$, E_{Pt}, and $E_{V_{In}/In_2O_3(111)}$ are energies of the $Pt/In_2O_3(111)$ surface, bulk Pt, and the $In_2O_3(111)$ surface with an In vacancy (V_{In}), respectively, so a more negative ΔE_{adh} value indicates a more stable SAC binding site.

Surface oxygen vacancy (V_O) sites were considered as the active sites for the In_2O_3 and Pt/In_2O_3 catalysts in CO_2 hydrogenation. Free energies of formation of V_O sites ($\Delta G_{f,V_O}$) by H_2 reduction were calculated from eqn (2)

$$\Delta G_{f,V_O} = E_{Surface\_V_O} + G_{H_2O} - E_{Surface} - G_{H_2} \quad (2)$$

where $E_{Surface\_V_O}$ and $E_{Surface}$ are energies of the $In_2O_3(111)$ or $Pt/In_2O_3(111)$ surfaces with and without a V_O site, respectively, and G_{H_2O} and G_{H_2} are free energies of molecular H_2O and H_2 including the experimental entropic corrections at the typical reaction temperature of 573 K. We assume that the additional components for the free energies of the $E_{Surface\_V_O}$ and $E_{Surface}$ should mostly cancel, so only their electronic energies are used. A V_O site with a higher $\Delta E_{f,V_O}$ may facilitate CO_2 adsorption and activation, although its formation by H_2 reduction will be more difficult. For surface-doped $Pt/In_2O_3(111)$, CO_2 adsorption and activation may mainly occur at the V_O site near the Pt site. These factors were considered when choosing the most favourable V_O site on each model surface for CO_2 hydrogenation, and the catalytic reaction network consists of CO_2 hydrogenation to CH_3OH and CO *via* the HCOO* and COOH* intermediates,

respectively, as well as the further hydrogenation of CO to CH_3OH.

The adsorption energy of an adsorbate A on a slab surface S is defined by eqn (3)

$$E_{ad}(A) = E_{total} - (E_{slab} + E_A) \quad (3)$$

where E_{total}, E_{slab}, and E_A are total electronic energies of the slab surface with the adsorbate, the clean slab surface, and the adsorbate as a free molecule, respectively. Adsorption energies of selected adsorbates such as CO_2, H_2 and CH_3OH are listed in Table S1 of the ESI.† Although the adsorption energies of H_2 and ln-CO_2 are low at 0 K, their surface coverages may be appreciable under high partial pressure conditions.

Similar to the study of Ye *et al.*,[42] the elementary step of the hydrogenation pathway usually involves the reaction of a single H adatom with the intermediate. We performed additional DFT calculations to study the effect of H migration[43] from the hydrogen adsorbed at the surrounding Pt/In sites to the In/O sites near the V_O site as shown in Fig. S22 and Table S16 (ESI†). In_2O_3(111) and Pt_{b_bulk} structures were found to have low energy barriers for H migration from one In to the other In (0.34 eV and 0.26 eV, respectively). The energy barriers for H migration from In to O are relatively high (1.18 eV and 1.14 eV, respectively). However, the $Pt_{b\_surface}$ model also has relatively high energy barriers for H migration from one In to another In and O (1.15 eV and 1.11 eV, respectively). Moreover, the presence of a second H adatom does not significantly affect the energy barriers of H migration for these three models. Therefore, we hypothesize that our above simplification of the hydrogenation steps should be reasonable.

We further examine the potential synergistic effect of the surface and bulk Pt dopants on the catalytic activity of the surface oxygen vacancy site. The In_2O_3(111) structure is doped with Pt atoms both at the surface and in the bulk (Pt_{b_dual}), where the main active site is the surface oxygen vacancy O_{b_vac} site, and the different pathways of the CO_2 hydrogenation reaction were calculated for this model as shown in Fig. S23–S26 (ESI†). Comparing the potential energy surfaces of the Pt_{b_dual} and $Pt_{b\_surface}$ models, the energy barriers of the elementary steps of CO_2 hydrogenation to methanol and the direct CO_2 dissociation pathway of the Pt_{b_dual} model are close to those of the $Pt_{b\_surface}$ model, while those of most elementary steps of CO hydrogenation to methanol and the CO_2 indirect dissociation pathway are higher than those of the $Pt_{b\_surface}$ model. Therefore, we focus this work on the single atom doping model.

Microkinetic simulations

The reaction pathways predicted from the DFT calculations for CH_3OH and CO formations from CO_2 hydrogenation were used to build a multisite microkinetic model for mean-field microkinetic simulations under typical experimental conditions for CO_2 hydrogenation using the CatMAP code.[44,45] Elementary steps in the microkinetic model are given in Table S8 (ESI†), where ''s'' and ''h'' denote the V_O and ''hydrogen reservoir'' sites, respectively. The structures of all the elementary steps are shown in Fig. S21 (ESI†). The ideal gas approximation and harmonic-rigid rotor approximation were employed for calculating the entropies and enthalpies of gaseous molecules and surface adsorbates, respectively. The degrees of rate control (DRC) and degrees of selectivity control (DSC)[46,47] proposed by Campbell and implemented in CatMAP were also calculated.

Catalytic preparation

Preparation of In_2O_3 catalyst. In_2O_3 sample was prepared by hydrothermal method. Briefly, 4.07 g of $In(NO_3)_3{\cdot}4.5H_2O$ was dissolved in 32 mL of deionized (DI) water under vigorous stirring. The alkali solution formed by 4 g of urea dissolved in 20 mL of DI water was added dropwise to the above solution, the resulting mixture was stirred vigorously for 2 h before kept in a Teflon-lined stainless autoclave at 393 K for 17 h. The precipitate was washed with DI water until the pH value reached 7, following by drying overnight at 333 K before calcination at 573 K for 5 h.

Preparation of Pt/In_2O_3 catalysts. To obtain platinum-promoted (0–3 wt% Pt) In_2O_3 catalysts by hydrothermal method. 2 g of $H_2PtCH_6{\cdot}6H_2O$ was first dissolved in 50 mL of DI water to form standard solution. The as-prepared Pt salt solution (0.63, 1.58, 4.74 g) and $In(NO_3)_3{\cdot}4.5H_2O$ (4.07 g) were dissolved in deionized (DI) water (32 mL) under vigorous stirring at room temperature. Then the solution formed by urea (2 g, 4 g, 8 g) dissolved in 20 mL DI water was added dropwise to the above solution. Other steps are the same as above for In_2O_3 catalyst preparation.

Preparation of Pt/In_2O_3-DI catalysts. 1Pt/In_2O_3-DI and 3Pt/In_2O_3-DI we prepared Pt/In_2O_3 by the dry impregnation method. $Pt(NO_3)_2$ solution (3.13 and 9.39 g) was added dropwise to the 3 g In_2O_3 before stirring evenly, the obtained samples were dried at 333 K for 12 h before calcined for 3 h at 573 K in static air.

Catalyst characterization

Powder X-ray diffraction (XRD) patterns were performed using a Rigaku Ultima IV powder diffractometer equipped with a Cu Kα radiation (λ = 0.15406 Å) operating at 40 kV and 40 mA. The diffractograms were obtained at a 2θ range of 0–90°.

The loadings of Pt in the samples were measured by inductively coupled plasma-optical emission spectrometry (ICP-OES) on an Agilent 720 spectrometer.

N_2 adsorption–desorption analyses were conducted at 77 K with a Micromeritics ASAP 2420 physisorption analyser. Before the measurement, the samples were outgassed at 300 °C for 10 h under vacuum, and then the surface area was calculated by the Brunauer–Emmett–Teller (BET) method.[48]

The microscopic features of the samples were characterized using a TEM (JEM-2100F) equipped with energy-dispersive X-ray spectroscopy (EDS) operated at 200 kV. The high-angle annular dark-field scanning TEM (HAADF-STEM) was performed using on a JEOL ARM300F equipped with double aberration correctors and a cold field emission gun.

CO_2 temperature-programmed desorption (CO_2-TPD) experiments were carried out with an OmniStar GSD320 02 mass spectrometer. First, the catalyst (100 mg) was pretreated at

573 K for 60 min in a flow of pure Ar or H_2. Then, the catalyst was saturated in flowing CO_2 at 323 K for 1 h followed by flushing in Ar for 3 h to remove any physiosorbed molecules. The CO_2-TPD measurement was then performed at 50–1023 K under continuous flow of Ar.

H_2 temperature-programmed reduction (H_2-TPR) was carried out on a Micromeritics ChemiSorb 2920 with a thermal conductivity detector (TCD). Typically, the catalyst sample (54 mg) was placed in a quartz reactor and pre-treated in flowing Ar at 423 K for 1 h. Then the temperature was raised from 323 to 973 K at a rate of 5 K min^{-1} with 5% H_2/Ar mixture gas.

Electron paramagnetic resonance (EPR) measurements of the free radicals were recorded by using 5,5-dimethyl-1-pyrroline (>99.0%) as a probe at a Bruker EMS-plus instrument (Bruker A300).

The X-ray absorption spectroscopy (XAS) experiments were conducted on the BL11B beamline of Shanghai Synchrotron Radiation Facility (SSRF). Before measurement, the samples were diluted by boron nitride and tableted. The data were collected at room temperature under fluorescence mode by using Lytle detector and the extended X-ray absorption fine structure (EXAFS) data were analysed *via* Athena software.

X-ray photoelectron spectrometer (XPS) analyses were performed using a Thermo Fisher Scientific ESCALAB 250Xi analyser with Al Kα radiation at 1486.6 eV under 9.9×10^{-7} torr. Binding energy values of all samples were calibrated based on an C 1s peak at 284.6 eV.

The synchrotron near-ambient pressure X-ray photoelectron spectroscopy (NAP-XPS) experiments were performed at beamline BL02B01 of SSRF. The C 1s photoemission line of C–C at 284.8 eV was used for the calibration. For the CO_2 hydrogenation reaction, sample were exposed to a mixture of H_2 (1.5 mTorr) and CO_2 (0.5 mTorr). For the Ar pretreatment, sample was in the environment of pure H_2 at 2 mTorr. For the H_2/Ar atmosphere, H_2 makes up 10% of all gases.

The *in situ* synchrotron-based vacuum ultraviolet photoionization mass spectrometry (SVUV-PIMS) study was carried out on the mass spectrometry endstation of the National Synchrotron Radiation Laboratory at Hefei, China. The Ar pretreatment products were monitored at an ionization energy of 11.8 eV, which allowed the detection of HCHO, CH_3OH and HCOOH. To detect the intermediates and products formed during CO_2 hydrogenation, the Ar pretreated Pt/In_2O_3 catalyst was exposed to H_2/CO_2 (3 : 1) at a flow rate of 80 mL min^{-1} and a pressure of 8 bar at 300 °C; the photoionization efficiency spectra were collected for 300 s at ionization energies in the range 10.6–11.6 eV in steps of 0.03 eV.

Catalytic evaluation

1.0 g of catalyst (40–60 mesh) with quartz sand mixing in equal volume was placed in a stainless-steel tube reactor. Prior to reaction, the sample was pretreated at 573 K for 1 h in pure Ar (150 mL min^{-1}) and then reactant gas mixture with a $H_2/CO_2/N_2$ ratio of 73/24/3 and a pressure of 5.0 MPa at 573 K was introduced into the reactor. The effluents were analysed online with a Shimadzu GC-2010C gas chromatograph equipped with thermal conductivity and flame ionization detectors. The CO_2 conversion was calculated by an internal normalization method. The catalytic performance after 48 h of reaction was typically used for discussion.

The CO_2 conversion denoted as $X(CO_2)$, CH_3OH selectivity denoted as $S(CH_3OH)$ and space-time yield (STY) of methanol denoted as $STY(CO_2)$ were calculated according to the following equations:

$$X(CO_2) = \frac{CO_{2\,inlet} - CO_{2\,outlet}}{CO_{2\,inlet}} \times 100\% \quad (4)$$

$$S(CH_3OH) = \frac{CH_3OH_{outlet}}{CO_{2\,inlet} - CO_{2\,outlet}} \times 100\% \quad (5)$$

$$STY(CH_3OH) = \frac{GHSV \times V_{\%}(CO_2) \times X(CO_2) \times S(CH_3OH) \times M(CH_3OH)}{22.4 \times 1000 \times m_{cat}} \times \left[g\ g_{cat}^{-1}\ h^{-1}\right] \quad (6)$$

Results

Active sites and reaction pathways on Pt/In_2O_3 SACs

The stoichiometric In_2O_3(111) surface shown in Fig. S1a (ESI†) has threefold symmetry, so its surface In and O atoms fall into six and four groups, labelled by In_a–In_f and O_a–O_d, respectively. The most stable single-atom Pt/In_2O_3(111) structures, with the Pt dopant located at the surface and in the bulk, are shown in Fig. 1a and b, respectively, based on the calculated ΔE_{adh} of a bulk Pt atom with the In_2O_3(111) slab in the presence of a V_{In}. As shown in Fig. 1c and Table S2 (ESI†), our calculations indicate that the Pt dopant preferably replaces the $In_{b\_surface}$ site for surface doping (denoted as $Pt_{b\_surface}$) and the In_{b_bulk} site for bulk doping (denoted as Pt_{b_bulk}). In both cases, the ΔE_{adh} values are substantially more negative than the cohesive energy of bulk Pt (ΔE_{coh}), suggesting the strong interaction of the single atom Pt dopant with the In_2O_3(111) slab, which may prevent the Pt dopants from self-aggregation.

Surface V_O sites are usually considered the active sites for CO_2 hydrogenation, and the V_O site, which has a higher $\Delta G_{f,VO}$, is usually suggested to have a higher CO_2 reactivity.[8] For the surface and bulk-doped Pt/In_2O_3(111) structures, the most favourable V_O sites further shown in Fig. 1a and b are located at the O_b and O_c sites (denoted as O_{b_vac} and O_{c_vac}), respectively. For the pristine In_2O_3(111) slab, the most favourable V_O site as displayed in Fig. S1b (ESI†) is situated at the O_c site (also denoted as O_{c_vac}). The most favourable V_O site was determined from the calculated $\Delta G_{f,VO}$ values of all surface V_O sites, as shown in Fig. 1d and Table S3 (ESI†), considering the Sabatier principle.[49] As noted above, a V_O site with a higher $\Delta G_{f,VO}$ value may interact more strongly with CO_2, resulting in a higher CO_2 reactivity, although its formation by H_2 reduction becomes thermodynamically and also possibly kinetically more

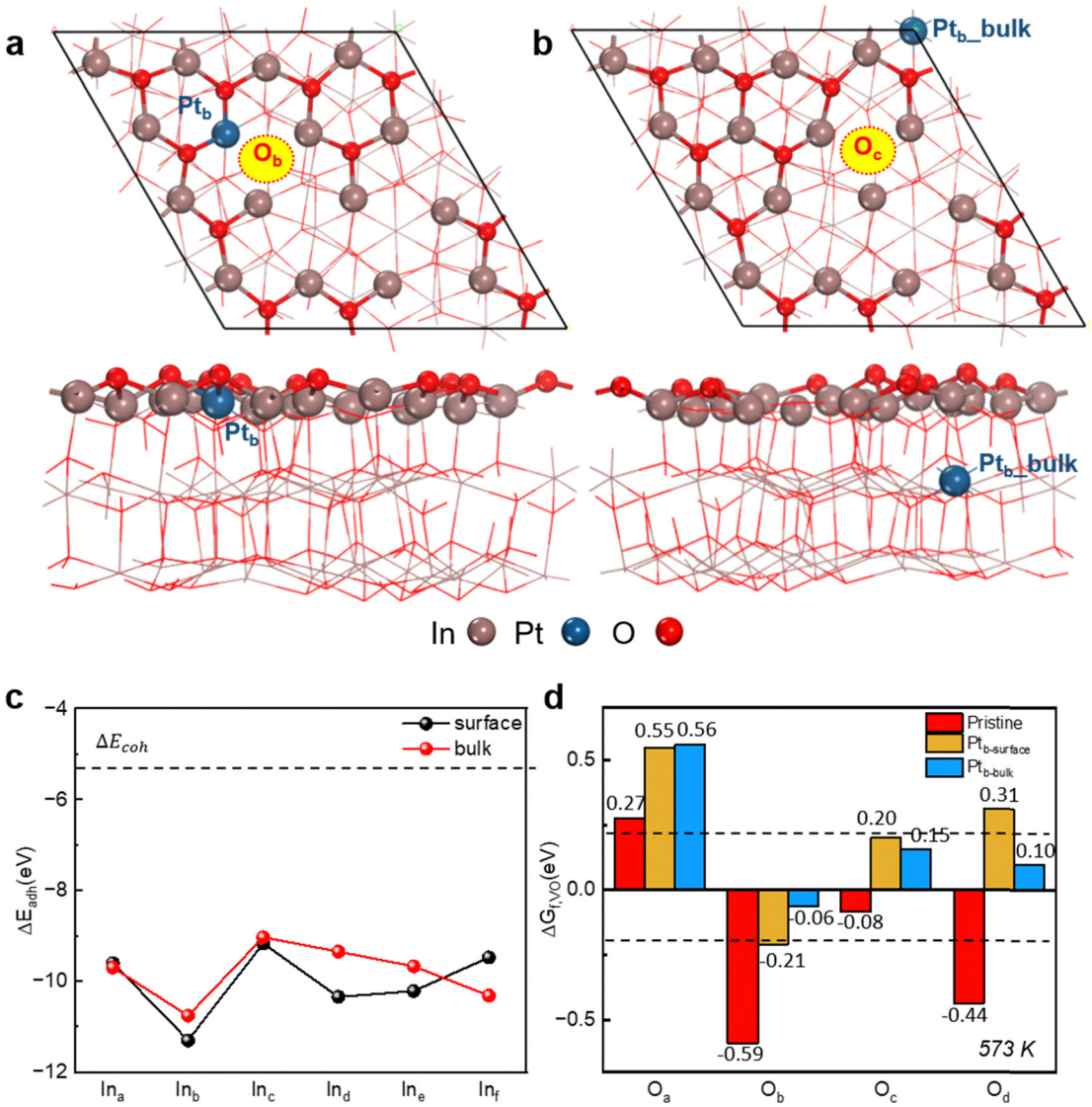

Fig. 1 Screening single atom-doped Pt/In_2O_3 catalyst structures and active sites. (a) Top and side views of the most stable surface-doped Pt/In_2O_3(111) structure with the Pt dopant located at the $Pt_{b\_surface}$ position and the surface oxygen vacancy (V_O) situated at the O_b site. (b) Top and side views of the most stable bulk-doped Pt/In_2O_3(111) structure with the Pt dopant located at the Pt_{b_bulk} position and the surface V_O site placed at the O_c site. (c) Calculated adhesive energies of a bulk-doped (red) or surface-doped (black) Pt atom with an In vacancy (V_{In}) in In_2O_3(111), which are compared with the cohesive energy of bulk Pt. (d) Calculated free formation energies of surface V_O on pristine (red), surface (yellow), and bulk (blue) doped Pt/In_2O_3(111) for H_2 reduction at 573 K. The dashed lines (±0.2 eV) represent a region of near thermoneutrality for the free formation energies considering the typical accuracies of DFT predictions.

difficult. Therefore, the most favourable V_O site should have the highest $\Delta G_{f,VO}$ value, provided that its formation by H_2 reduction is exothermic or nearly thermoneutral at the typical reaction temperature, as indicated by the dashed lines in Fig. 1d. For the surface-doped Pt/In_2O_3(111) model, the O_{b_vac} site adjacent to the $Pt_{b\_surface}$ site is chosen, as CO_2 prefers to adsorb at the $Pt_{b\_surface}$–O_{b_vac} dual site. As shown in Fig. 1d, introducing the Pt dopant either at the surface or in the bulk of the In_2O_3(111) slab substantially increases the $\Delta G_{f,VO}$ values for all four types of surface V_O sites, which can be attributed to the deeper reduction of the metal sites surrounding the V_O site (Fig. S2 and S3, ESI†). Surface doping of In_2O_3(111) leads to a deeper reduction of the three metal sites around the O_{b_vac} site, which suggests a lower stability, consistent with the increase in the $\Delta G_{f,VO}$ value from −0.59 eV of the pristine In_2O_3(111) to −0.21 eV upon introducing the $Pt_{b\_surface}$ dopant. Similarly, a deep reduction also occurs at three metal sites around the O_{c_vac} site in the bulk-doped Pt/In_2O_3 model, which corresponds to an increase in the $\Delta G_{f,VO}$ value from the pristine In_2O_3(111) of −0.08 eV to 0.15 eV upon Pt doping.

The optimized structures of the important reaction intermediates for CO_2 hydrogenation to CH_3OH and CO over the surface and bulk-doped Pt/In_2O_3(111) models are presented in Fig. S4–S6 (ESI†), with their calculated adsorption energies summarized in Table S1 (ESI†). At the O_c_vac site on the pristine In_2O_3(111) surface, CO_2 can weakly physisorb in the

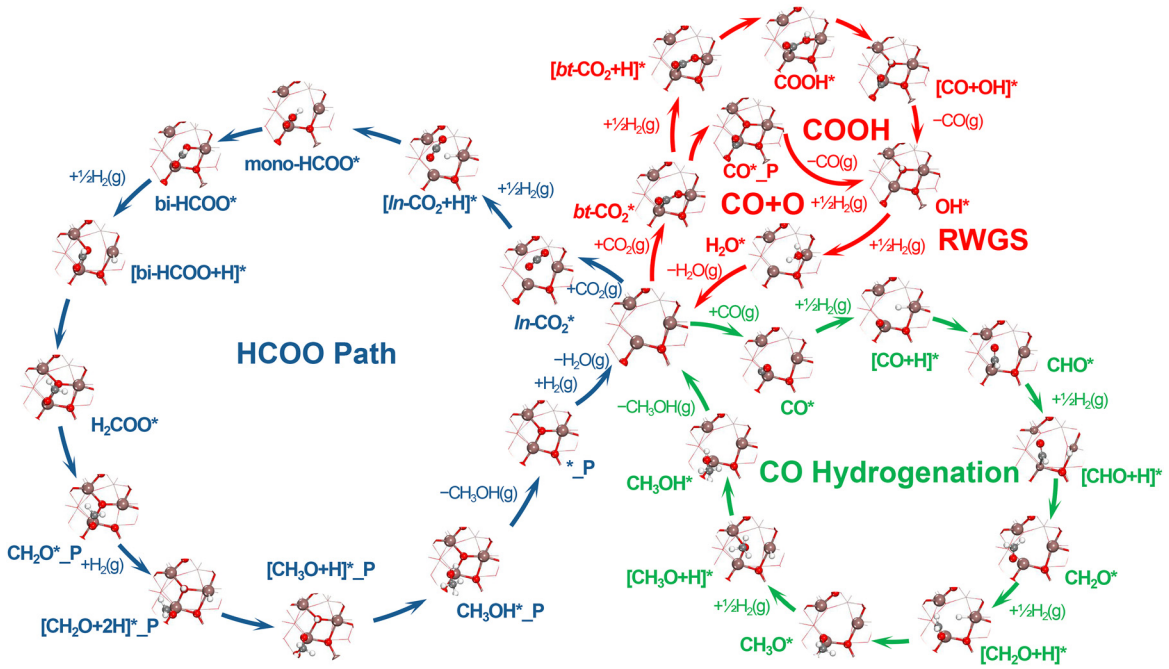

Fig. 2 Catalytic cycles for CO_2 hydrogenation to CH_3OH and CO over Pt/In_2O_3 SACs. Methanol can form directly from CO_2 hydrogenation *via* the HCOO pathway (blue), or indirectly from the CO intermediate *via* CO hydrogenation (green), whereas CO can form by direct CO_2 dissociation or indirectly by the COOH route (red). _D* and _P* represent the defective and perfect structures with and without an oxygen vacancy, respectively.

ln-CO_2* structure or chemisorb in the bt-CO_2* structure. Surface Pt doping greatly strengthens CO_2 chemisorption at the $Pt_{b\_surface}$–O_{b_vac} site in the bt-CO_2* structure by approximately 1.9 eV, so its CO_2 adsorption energy changes from being quite endothermic to quite exothermic. Similarly, CO adsorption at the $Pt_{b\_surface}$ site on the surface-doped $Pt/In_2O_3(111)$ is also much stronger than that at the O_{c_vac} site on the pristine $In_2O_3(111)$ surface by 0.8 eV. In contrast, bulk Pt doping only slightly affects the adsorption energies of the various species at the Pt_{b_bulk}–O_{c_vac} site by <0.2 eV, when compared with those at the O_{c_vac} site on the pristine $In_2O_3(111)$ surface. Thus, our calculations show that surface and bulk Pt doping result in distinct impacts on the adsorption properties of Pt/In_2O_3 SACs. Fig. 2 shows the entire reaction network for CO_2 hydrogenation to CH_3OH and CO over the Pt/In_2O_3 SACs. Our calculations show that CH_3OH can form directly *via* the HCOO pathway from stepwise CO_2 hydrogenation, or indirectly *via* the CO hydrogenation pathway from the CO intermediate, which can be produced by direct CO_2 dissociation or indirectly *via* the COOH pathway. Our predicted reaction pathways for CO_2 hydrogenation to CH_3OH and CO are generally consistent with those found in the recent literature for related catalysts.[12,50]

Fig. S7 (ESI†) compares the energy profiles of CH_3OH formation from direct CO_2 hydrogenation *via* the HCOO pathway (the blue cycle in Fig. 2), with the detailed relative energies given in Table S4 (ESI†). Compared with the relative energies for the pristine $In_2O_3(111)$ surface, those for the surface-doped $Pt/In_2O_3(111)$ model are less negative, whereas those for the bulk-doped $Pt/In_2O_3(111)$ model are more negative except for the HCOO* and $[CH_2O + 2H]$* intermediates. Relative energies of most reaction intermediates and energy barriers of most transition states for the HCOO pathway at the $Pt_{b\_surface}$–O_{b_vac} site on the $Pt_{b\_surface}$ model are the highest, and the rate-determining step (RDS) is CH_3O* hydrogenation to CH_3OH* with an energy barrier of 2.49 eV. The RDS at the Pt_{b_bulk}–O_{c_vac} site on the Pt_{b_bulk} model is HCOO* hydrogenation to H_2COO* with an energy barrier of 0.69 eV, indicating that the bulk-doped model is beneficial for methanol formation *via* the HCOO* pathway.

Fig. S8 and S9 (ESI†) show the energy profiles for CO formation from CO_2 direct dissociation and *via* the indirect COOH pathway (red cycle in Fig. 2), with the detailed relative energies given in Tables S5 and S6 (ESI†). The potential energies of the CO_2 direct dissociation pathway are generally lower than those of the indirect COOH pathway, suggesting the former to potentially play a more important role than the latter in CO formation. Furthermore, compared with the energy profiles for the pristine $In_2O_3(111)$ surface, those for the surface-doped $Pt/In_2O_3(111)$ model are more downhill, whereas those for the bulk-doped $Pt/In_2O_3(111)$ are more uphill, indicating that CO formation may be suppressed and accelerated by surface and bulk Pt doping, respectively.

Fig. S10 (ESI†) compares the energy profiles for CH_3OH formation from the CO intermediate *via* the CO hydrogenation pathway (the green cycle in Fig. 2), with the detailed relative energies given in Table S7 (ESI†). Compared with the potential energies for the pristine $In_2O_3(111)$ surface, those for the surface-doped $Pt/In_2O_3(111)$ model are lower, whereas those for the bulk-doped $Pt/In_2O_3(111)$ model are rather similar, implying that bulk Pt doping has a less pronounced effect on

this route than surface Pt doping. The RDS at the $Pt_{b\_surface}$–O_{b_vac} site on the $Pt_{b\text{-}surface}$ model is CH_3O^* hydrogenation to CH_3OH^* with an energy barrier of 1.37 eV, and that at the Pt_{b_bulk}–O_{c_vac} site on the $Pt_{b\text{-}bulk}$ model is CH_2O^* hydrogenation to CH_3O^* with an energy barrier of 1.23 eV. From the energy barrier of the RDS, compared with the $Pt_{b\text{-}surface}$ model, the Pt_{b_bulk} model may be more favorable for CO hydrogenation to CH_3OH.

For the CO_2 hydrogenation pathway on the $In_2O_3(111)$ surface, the earlier study of Frei *et al.*[11] indicates that HCOO* is formed by hydrogenation of the chemisorbed carb-CO_2* with an energy barrier of 0.44 eV, whereas in our work, it is formed by hydrogenation of the physisorbed ln-CO_2* with a much lower energy barrier of 0.01 eV. In addition, our previous calculations[12,41] suggest carb-CO_2* is a spectator species. carb-CO_2* protonation to CO_2OH^* must overcome an energy barrier of 0.72 eV, whereas the reverse reaction has a much lower energy barrier of 0.25 eV, indicating that it is kinetically more favourable for CO_2OH^* dissociation back to the carb-CO_2*, *i.e.*, the reaction is endoergic. Furthermore, CO_2OH^* dissociation to [ln-CO_2 + OH]* needs to overcome an energy barrier of 0.61 eV, which is higher than that for CO_2OH^* dissociation back to the carb-CO_2* of 0.25 eV. The above two findings indicate that carb-CO_2* is a spectator species. Finally, our previous calculations[41] also suggest carb-CO_2* hydrogenation to the bi-HCOO* to be kinetically unfavourable with an energy barrier of 1.01 eV.

The previous work of Cannizzaro *et al.*[23] focused on Ni-promoted In_2O_3 catalysts using the Ni_1-doped, Ni_1-adsorbed, and Ni_8-cluster models. For CO_2 hydrogenation in the HCOO* pathway, the RDS for the Ni_1-doped model is HCOO* hydrogenation to H_2COO^* with a high energy barrier of 3.26 eV, whereas the energy barrier of this step for the $Pt_{b\_surface}$ model is much lower at 0.55 eV. On the other hand, the RDS on the surface-doped Pt/In_2O_3 model is CH_3O^* hydrogenation to CH_3OH^* with an energy barrier of 2.49 eV, whereas the energy barrier of this step for the Ni_1-doped model is much lower at 1.02 eV from their calculations.[23] In addition, for the Ni_1-doped model, their calculations[23] show that the CH_2O^* intermediate is obtained from H_2COOH^* dissociation, and the subsequent cleavage of the C–O bond in H_2COOH^* yields CH_2O^* and OH* with an energy barrier of 1.01 eV. In comparison, for the $Pt_{b\_surface}$ model, our calculations show that CH_2O^* is formed by H_2COO^* dissociation with an energy barrier of 1.34 eV. For CO formation *via* the CO_2 direct dissociation pathway, they predicted an energy barrier of 2.40 eV for the Ni_1-doped model,[23] which is rather similar to that of 2.71 eV for the $Pt_{b\_surface}$ model from our calculations. However, they did not study the CO_2 indirect dissociation pathway *via* the COOH* intermediate for the Ni_1-doped model.[23] For the $Pt_{b\_surface}$ model, our calculations show that the RDS is CO_2 hydrogenation to COOH* with an energy barrier of 1.70 eV, considerably lower than that for the CO_2 direct dissociation pathway. The above comparison thus indicates that despite the apparent similarity between the catalyst model and the metal dopant for the surface-doped Ni/In_2O_3 and Pt/In_2O_3 SACs, the energy barriers of the elementary steps and the identity of the RDS can be quite different especially for CH_3OH formation *via* the HCOO pathway.

Microkinetic simulations of CO_2 hydrogenation on Pt/In_2O_3 SACs

For quantitative prediction of the catalytic performance of the Pt/In_2O_3 SACs, multisite mean-field microkinetic simulations using our DFT energetics were performed; all the reaction routes shown in Fig. 2 were included in the microkinetic models. Fig. 3a shows the calculated turnover frequencies (TOFs) for CO_2 consumption under the typical reaction conditions of 473–673 K and 5 MPa ($H_2:CO_2 = 3:1$). We predict that the Pt_{b_bulk}–O_{c_vac} and $Pt_{b\_surface}$–O_{b_vac} sites exhibit considerably higher and lower CO_2 reactivity, respectively, indicating that bulk Pt doping, not surface Pt doping, may facilitate the CO_2 hydrogenation reaction. Fig. 3b further displays the calculated CH_3OH selectivities under the above reaction conditions, which consistently decrease as the reaction temperature increases for all three model surfaces. For the pristine $In_2O_3(111)$ surface, we predict that the CH_3OH selectivity decreases from ~97% at 523 K to ~85% at 573 K, in reasonable agreement with the experimental observations for the pure In_2O_3 catalyst described in the following section. The bulk-doped $Pt/In_2O_3(111)$ model is predicted to exhibit a very similar profile for the CH_3OH selectivity in the simulated temperature range, whereas the surface-doped $Pt/In_2O_3(111)$ model is found to clearly favour CO formation with a very low CH_3OH selectivity even at the low reaction temperature of 473 K. Further simulations were performed to study the effect of Pt loading on CO_2 reactivity and CH_3OH selectivity at 573 K for the bulk-doped $Pt/In_2O_3(111)$ model as shown in Fig. 3c, indicating that at a relatively low reaction temperature, increasing the Pt loading for bulk doping may enhance the CO_2 reactivity 100× without significantly lowering CH_3OH selectivity.

Fig. 3d shows the calculated DRC for CO_2 consumption at the O_{c_vac} site on the pristine $In_2O_3(111)$ surface, indicating a strong dependence of the DRCs on reaction temperature. At relatively low reaction temperatures from 473 K to 598 K, the DRC of H_2CO^* hydrogenation to H_3CO^* (R6) is the largest, suggesting that this elementary step is the rate-determining step, and that lowering this energy barrier will lead to higher CO_2 reactivity. At a higher reaction temperature, OH* hydrogenation to H_2O^* to form an oxygen vacancy (R11) is the RDS, whereas lowering the energy barrier of H_2CO^* hydrogenation to H_3CO^* has a much less pronounced effect on the overall CO_2 reactivity. Fig. 3e displays the calculated DRC values for the CO_2 reaction rate at the $Pt_{b\_surface}$–O_{b_vac} site on the surface-doped $Pt/In_2O_3(111)$ model. CO_2* direct dissociation (R14) is the RDS for CO_2 conversion at 473–673 K, suggesting that lowering its energy barrier should lead to higher CO_2 reactivity. This result is consistent with the very high energy barrier of 2.71 eV for CO_2 direct dissociation on the surface-doped $Pt/In_2O_3(111)$ model (Fig. S8 and Table S5, ESI†), although the bt-CO_2* structure has a very negative adsorption energy of −0.78 eV. On the other hand, the DRCs of the elementary steps related to CH_3OH formation are consistently low above 473 K, as the product

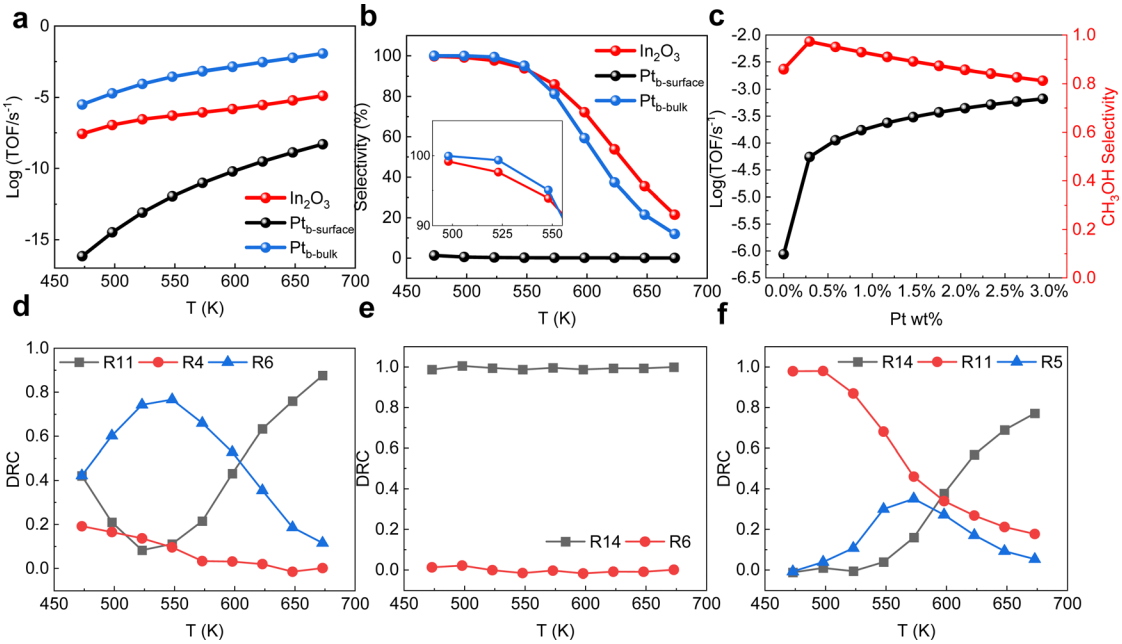

Fig. 3 Microkinetic simulations of the catalytic performance of Pt/In_2O_3 SACs. (a) and (b) Plots of the calculated turn-over frequencies (TOFs) for CO_2 consumption (a) and CH_3OH selectivities (b) for CO_2 hydrogenation over the pristine In_2O_3(111) surface (black) and the surface and bulk-doped Pt/In_2O_3(111) models (red and blue, respectively) under the reaction conditions of 473–673 K, 5 MPa, and $H_2 : CO_2 = 3 : 1$. (c) Plots of simulated TOFs for CO_2 consumption (black) and CH_3OH selectivities (red) for CO_2 hydrogenation over the bulk-doped Pt/In_2O_3(111) model catalyst at different Pt loadings at 573 K. (d)–(f) Calculated DRC for the elementary steps during CO_2 hydrogenation over the pristine In_2O_3(111) surface (d) and the surface and bulk-doped Pt/In_2O_3(111) models (e and f, respectively).

composition is dominated by CO. Fig. 3f further shows the calculated DRCs for the CO_2 reaction rate at the Pt_{b_bulk}–O_{c_vac} site on the bulk-doped Pt/In_2O_3(111) model. Below 600 K, the DRCs of the OH* hydrogenation to generate the V_O site (R11) are largest, suggesting V_O formation to be the rate determining step, consistent with the much higher free formation energy of the O_{c_vac} site on this surface (Fig. 1d). This also agrees with the calculated coverages of the surface species shown in Fig. S11c (ESI†), suggesting that the free sites are mostly occupied by OH* at relatively low temperatures. At higher reaction temperatures, the DRC of direct CO_2* dissociation (R14) becomes largest, as CO becomes the main product. The calculated DSC for CH_3OH shown in Fig. S12 (ESI†) are also very sensitive to the reaction temperature, especially for the pristine In_2O_3(111) surface and the bulk-doped Pt/In_2O_3(111) model.

To reveal the effect of Pt doping on the electronic structure of the In site on the catalyst surface, projected density of states (PDOS) analysis was performed for the relevant structures. As shown in Fig. S13a (ESI†) for the In_c site in the presence of both H* and HCOO* adsorbates, the PDOS of the various In_c orbitals as well as the H* orbitals are all shifted to lower energies upon introducing a bulk Pt dopant. Similar observations were made for the effects of the bulk Pt dopant on the PDOS of the In_c orbitals without the presence of either the H* or HCOO* adsorbate, suggesting that introducing the bulk Pt dopant has significant influence on the redox property of the surface In_c site. Meanwhile, as discussed earlier, the Bader charge analyses shown in Fig. S2 and S3 (ESI†) suggest a deeper reduction of the three In sites around the O_{c_vac} site upon introduction of the bulk Pt dopant, consistent with an increase in the $\Delta G_{f,VO}$ value.

Furthermore, crystal orbital Hamilton population (COHP) and integrated COHP (ICOHP) analyses were also performed as shown in Fig. S13b (ESI†) to understand the effect of the bulk Pt dopant on the interaction between In_c and H* in the presence of HCOO*. The increase in the negative ICOHP value at the Fermi surface indicates that introducing the bulk Pt dopant will strengthen the orbital interaction between In_c and H*, consistent with the predicted stronger H* adsorption and the lower effective energy barrier of HCOO* hydrogenation (Table S4, ESI†), leading to enhanced reactivity of the bulk-doped In_2O_3 catalyst. However, CO_2 adsorption on the surface-doped Pt/In_2O_3(111) model is too strong, leading to much higher energy barriers for its subsequent hydrogenation. Whereas the RDS step in the HCOO pathway for the Pt_{b_bulk} model is HCOO* hydrogenation to H_2COO* with a modest energy barrier of 0.69 eV, that for the $Pt_{b\_surface}$ model is CH_3O* hydrogenation to CH_3OH* with a much higher energy barrier of 2.49 eV.

The formal oxidation states of the Pt single atom sites in the surface-doped and bulk-doped Pt/In_2O_3 models are estimated to be both +3.5 based on the calculated Bader charges, when compared with those of bulk Pt and its various oxides as shown in Fig. S13b and Table S14 (ESI†). Upon the formation of a V_O on the surface, the formal oxidation states of the Pt single atom sites in the surface-doped and bulk-doped Pt/In_2O_3 models become +1.9 and +3.5, respectively. Thus, the formal oxidation

state of the surface-doped Pt is significantly affected by the formation of the nearby V_O, as the Bader charge of $Pt_{b\_surface}$ significantly decreases from 1.40 $|e|$ to 0.81 $|e|$ upon the formation of O_{b_vac} near $Pt_{b\_surface}$ (Fig. S2, ESI†). In contrast, the formation of a surface V_O on the bulk-doped Pt/In_2O_3 model has little effect on the formal oxidation state of the bulk Pt dopant, whose Bader charge remains essentially the same at 1.39 $|e|$. Therefore, our DFT-based microkinetic simulations show that selectively introducing bulk Pt dopants to the In_2O_3 catalyst can greatly enhance CH_3OH productivity by substantially increasing CO_2 reactivity while largely maintaining CH_3OH selectivity, which suppresses the RWGS activity usually promoted by surface Pt dopants.

Preparation and catalytic performance of Pt-modified In_2O_3

Based on our theoretical predictions, a series of In_2O_3 and Pt/In_2O_3 samples with different Pt contents were synthesized by the hydrothermal method.[8] The actual Pt loadings of the Pt/In_2O_3 samples were measured by ICP-OES to be 0.44, 1.24 and 2.82 wt%, denoted as $0.5Pt/In_2O_3$, $1Pt/In_2O_3$ and $3Pt/In_2O_3$ catalysts, respectively. For comparison, $1Pt/In_2O_3$-DI and $3Pt/In_2O_3$-DI samples with similar Pt concentrations of 1.37 and 3.01 wt%, respectively, were also prepared by the dry impregnation method, in which the Pt species are mostly present on the In_2O_3 surface. Comparative analysis of surface sensitive XPS and ICP-OES results reveals that compared to $1Pt/In_2O_3$-DI and $3Pt/In_2O_3$-DI, the Pt species in the $1Pt/In_2O_3$ and $3Pt/In_2O_3$ catalysts are mostly distributed in the bulk of In_2O_3 (Fig. 4a). CO chemisorption provides further evidence that Pt on $1Pt/In_2O_3$ and $3Pt/In_2O_3$ mainly exists in the bulk phase (Table S9, ESI†).

Compared to the pristine In_2O_3 catalyst, all Pt-doped In_2O_3 catalysts show much higher activity and methanol yields at 573 K. With increasing Pt content, the CO_2 conversion increased significantly to 25.1% over $3Pt/In_2O_3$, which is nearly three times that achieved with pristine In_2O_3 (8.8%). The methanol selectivity decreased slightly from 75.2% over In_2O_3 to approximately 70% over $1Pt/In_2O_3$ (Fig. 4b), consistent with our theoretical predictions in Fig. 3b, and then decreased sharply to 46.8% for $3Pt/In_2O_3$. The STY of methanol for $1Pt/In_2O_3$ is as high as 0.41 g g_{cat}^{-1} h^{-1} with a CO_2 conversion of 18.9%, which is more than twice that of In_2O_3. The STY of methanol was further enhanced by increasing the GHSV, and that for the $1Pt/In_2O_3$ catalyst reached 1.25 g g_{cat}^{-1} h^{-1} with a methanol selectivity of 84.8% at 54 000 mL g_{cat}^{-1} h^{-1} (Fig. 4c). Fig. 4f and Table S10 (ESI†) show that $1Pt/In_2O_3$ and $3Pt/In_2O_3$

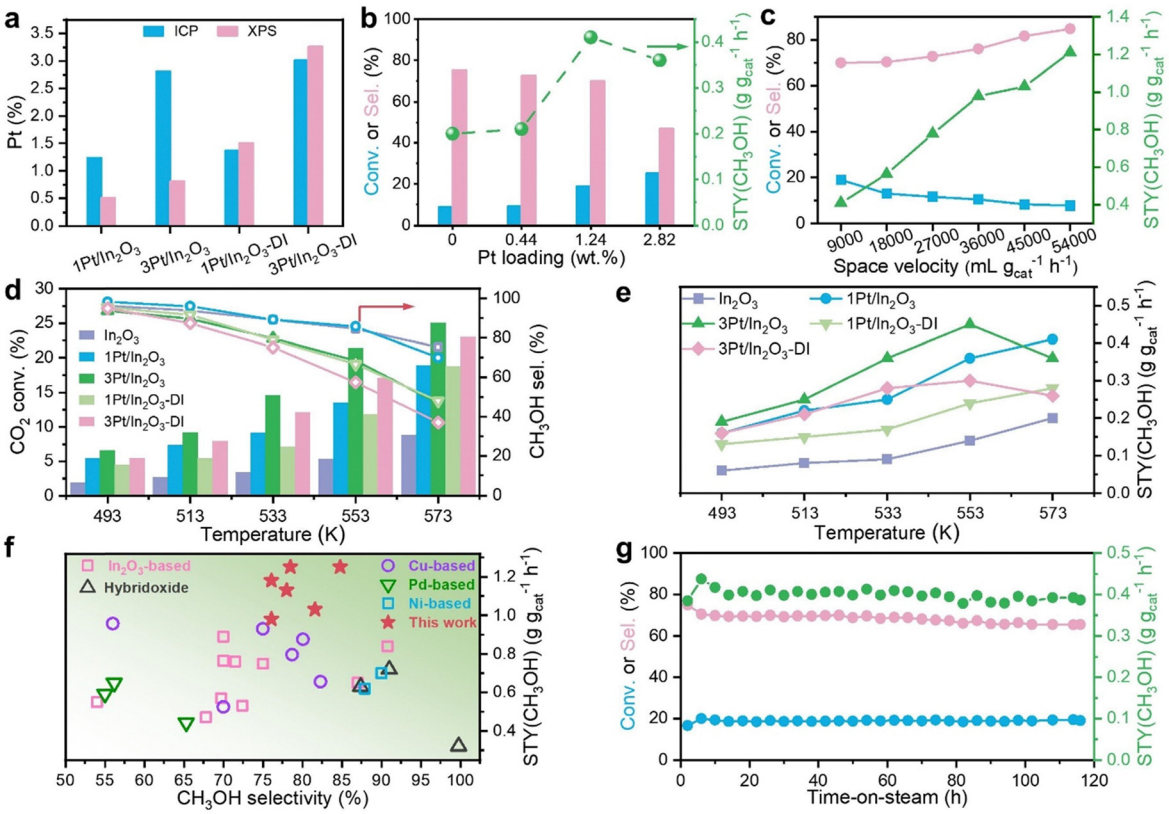

Fig. 4 Catalytic properties of In_2O_3 and various Pt-modified In_2O_3 catalysts. (a) Pt contents of various catalysts characterized *via* ICP and XPS. (b) Effects of Pt content on CO_2 conversion and methanol selectivity over Pt modified In_2O_3 catalysts prepared by the hydrothermal method. (c) Catalytic performance of $1Pt/In_2O_3$ under different space velocities. (d) and (e) Comparison of CO_2 conversion, methanol selectivity (d) and methanol yield (e) as a function of temperature over In_2O_3 and various Pt-modified In_2O_3 catalysts. (f) Comparison of the STY and selectivity of methanol over the $1Pt/In_2O_3$ and $3Pt/In_2O_3$ samples in this work and other state-of-the art catalysts (see Table S8 for more details, ESI†). (g) Stability test of $1Pt/In_2O_3$ under standard reaction conditions (5 MPa, 573 K, H_2/CO_2 = 3 : 1, GHSV = 9000 mL g_{cat}^{-1} h^{-1}).

delivered high STYs of methanol together with high methanol selectivity compared with various metal-modified In_2O_3 and other state-of-the-art catalysts reported in the literature under similar reaction conditions.[5,15,16,51–63]

The catalytic performances of 1Pt/In_2O_3-DI and 3Pt/In_2O_3-DI are much worse than those of bulk-doped 1Pt/In_2O_3 and 3Pt/In_2O_3, respectively, especially above 513 K (Fig. 4d and e). The methanol selectivity of 1Pt/In_2O_3 is nearly identical to that of In_2O_3 in the entire temperature range studied, whereas 3Pt/In_2O_3 has much lower methanol selectivity, similar to 1Pt/In_2O_3-DI, suggesting that the high Pt content in 3Pt/In_2O_3 may also increase the content of surface Pt doping. As the reaction temperature increases, the methanol selectivity over 1Pt/In_2O_3-DI decreases more rapidly than that over 1Pt/In_2O_3, consistent with our theoretical predictions. Compared with 1Pt/In_2O_3 and 1Pt/In_2O_3-DI, the increase in the CO_2 conversion over 3Pt/In_2O_3 and 3Pt/In_2O_3-DI is slower with increasing temperature, resulting in a lower STY of methanol at 573 K. Arrhenius plots for methanol formation in Fig. S14b (ESI†) show that the apparent activation energy for methanol formation for 1Pt/In_2O_3 and 3Pt/In_2O_3 are 54.0 and 50.5 kJ mol^{-1}, respectively, which are lower than those for 1Pt/In_2O_3-DI (61.8 kJ mol^{-1}) and 3Pt/In_2O_3-DI (68.9 kJ mol^{-1}). This also indicates that bulk-doped 1Pt/In_2O_3 and 3Pt/In_2O_3 are kinetically more favourable with lower energy barriers for methanol synthesis. Moreover, the CO_2 conversion and methanol yield over 1Pt/In_2O_3-DI decrease rapidly from 13.0% and 0.26 g g_{cat}^{-1} h^{-1} at 16 h, respectively, to 10.7% and 0.20 g g_{cat}^{-1} h^{-1} at 118 h (Fig. S14e, ESI†). A significant deactivation was also detected for 3Pt/In_2O_3-DI (Fig. S14f, ESI†). However, the catalytic performance remains almost constant throughout the 118 h reaction for In_2O_3, 1Pt/In_2O_3 and 3Pt/In_2O_3 (Fig. 4g and Fig. S14c, d, ESI†).

Characterizations of Pt-modified In_2O_3

For samples prepared by the hydrothermal method, the specific surface area significantly increases to 126 m^2 g^{-1} for 3Pt/In_2O_3 (Fig. S15a and b, ESI†). In contrast, the surface areas of 1Pt/In_2O_3-DI and 3Pt/In_2O_3-DI are much lower than In_2O_3, indicating that the Pt species might block the pores (Table S9, ESI†). Lattice fringes identified at multiple locations in the HRTEM images of all the samples yield a *d*-spacing of 0.292 nm, corresponding to the (222) planes of In_2O_3 (Fig. S16a and b, ESI†).

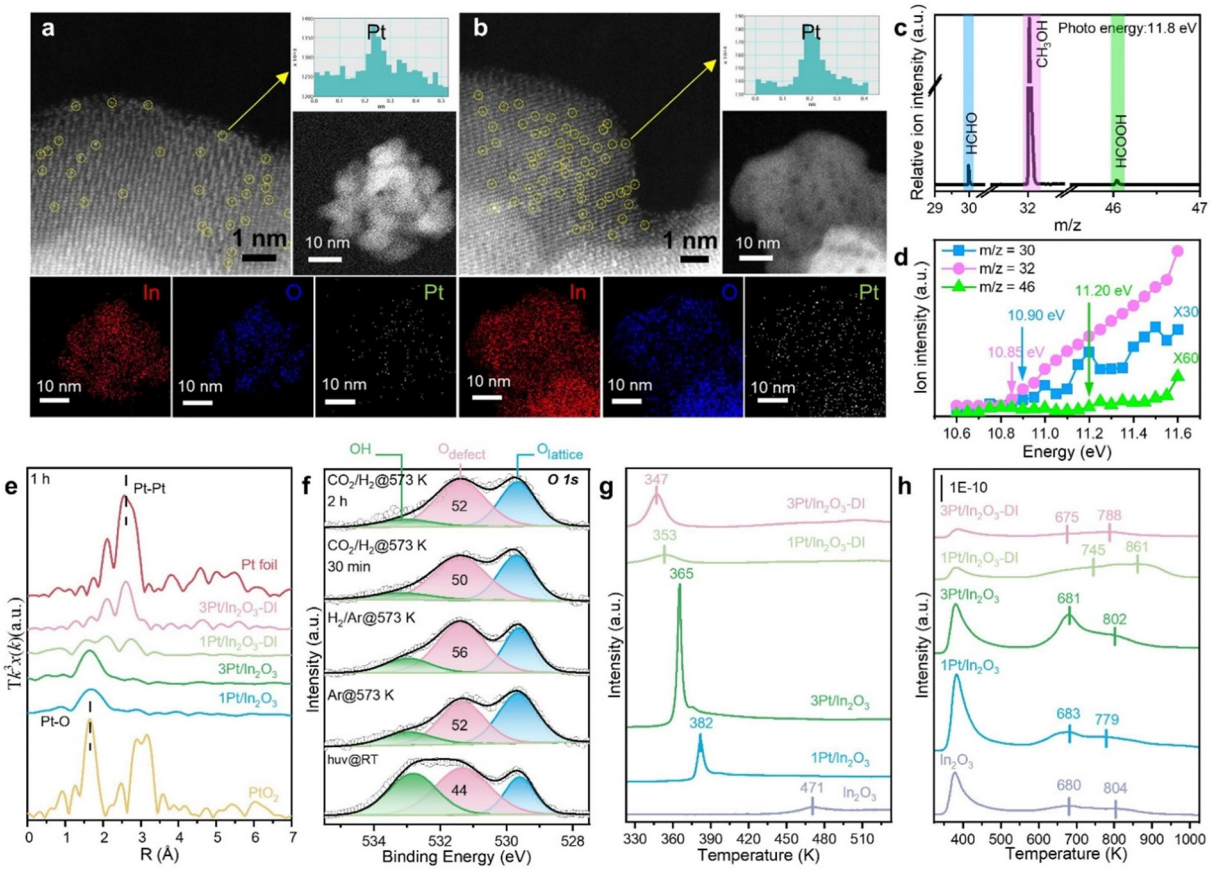

Fig. 5 Characterization of various catalysts. (a) and (b) HAADF-STEM images with the corresponding line-scanning intensity profiles obtained on the magnified areas and the TEM-EDS elemental mappings of 1Pt/In_2O_3 (a) and 3Pt/In_2O_3 (b). (c) *In situ* SVUV-PIMS detection of gas-phase products during the CO_2 hydrogenation process. (d) Photoionization efficiency spectra of the signals of *m*/*z* 30, 32 and 46 during the CO_2 hydrogenation process. (e) The k^3-weighted Fourier transform of EXAFS spectra of Pt modified In_2O_3 catalysts after the CO_2 hydrogenation reaction for 1 h. (f) The *in situ* NAP-XPS spectra collected in the simulated reaction process. (g) and (h) H_2-TPR (g) and CO_2-TPD (h) profiles of pristine In_2O_3 and various Pt-modified In_2O_3 catalysts pretreated in Ar at 573 K for 1 h.

As shown in Fig. S15c (ESI†), only the XRD peaks of the body-centred cubic In_2O_3 crystalline lattice were observed for all samples. No characteristic diffraction peaks of Pt species were detected, suggesting that the Pt species are highly dispersed on the In_2O_3, which is attributed to the strong interaction between Pt and In_2O_3. This is further confirmed by aberration-corrected HAADF-STEM characterization, which showed no obvious Pt nanoparticles (Fig. 5a and b). EDS mappings reveal that Pt is uniformly dispersed throughout the sample. No Pt–Pt contribution, but only the Pt–O contribution is observed by the EXAFS spectroscopy at the Pt L_3-edge for all fresh samples (Fig. S17a, ESI†), indicating that the Pt species exist predominantly as isolated atoms, consistent with the HAADF-STEM observations. The fitted Pt–O coordination numbers (CNs) for 1Pt/In_2O_3-DI and 3Pt/In_2O_3-DI are 4.1 and 3.8, respectively (Table S11, ESI†), consistent with the surface-doped Pt/In_2O_3(111) model. These coordination numbers are lower than those for 1Pt/In_2O_3 (CN = 4.7) and 3Pt/In_2O_3 (CN = 4.4). X-ray absorption near edge structure spectra in Fig. S17c (ESI†) show that the white-line intensities for the 1Pt/In_2O_3-DI and 3Pt/In_2O_3-DI samples are similar to those of PtO_2, whereas those for the 1Pt/In_2O_3 and 3Pt/In_2O_3 are between those of Pt foil and PtO_2, indicating the oxidation state of Pt species (Pt^{n+}, $0 < n < 4$).[24,64] The Pt $4d_{5/2}$ XPS peak can be deconvoluted into three peaks located at 314.2, 315.3 and 317.0 eV (Fig. S18, ESI†), belonging to Pt^0, Pt^{2+} and Pt^{4+}, respectively.[21] The atomically dispersed Pt species in the fresh and thermally pretreated samples carry significant amounts of positive charges. These Pt^{n+} (Pt^{2+} and Pt^{4+}) cations may thus replace the In^{3+} ions in the In_2O_3 lattice or occupy the interstitial sites of 1Pt/In_2O_3 and 3Pt/In_2O_3, strongly binding with lattice O^{2-}. For 1Pt/In_2O_3-DI and 3Pt/In_2O_3-DI, the Pt^{n+} cations may be located at defect sites on the In_2O_3 surface.

When the SACs were exposed to reducing conditions, the interaction between the metal atoms and the support usually became weaker, resulting in aggregation of the metal atoms.[18] Notably, the Pt species in 1Pt/In_2O_3 and 3Pt/In_2O_3 remain in the Pt^{n+} oxidation state after reaction for 48 h (Fig. S17b and e, ESI†), although the Pt–O CN significantly decreases to 2.4 for 1Pt/In_2O_3 and 2.3 for 3Pt/In_2O_3 (Table S11, ESI†). Additionally, a lack of Pt–Pt bonds also confirms the atomic dispersion of Pt species in the spent 1Pt/In_2O_3 and 3Pt/In_2O_3 SACs. These results indicate the very high stability of the Pt SACs even at a high Pt loading of 2.82 wt%. For the spent 1Pt/In_2O_3 and 3Pt/In_2O_3, the Pt–O bond distance remains close to that in PtO_2, suggesting strong interactions between Pt and In_2O_3. However, the Pt species in 1Pt/In_2O_3-DI and 3Pt/In_2O_3-DI were obviously reduced to metallic Pt (Fig. S17b, d and e, ESI†), as Pt–Pt bonds originated from the sintering of surface Pt atoms were formed after reaction for only 1 h (Fig. 5e), which promotes the RWGS reaction. In addition, based on the Pt 4d XPS spectra of 1Pt/In_2O_3-DI and 3Pt/In_2O_3-DI, the Pt^0 peak appeared after reaction for only 1 h, further confirming the aggregation of Pt species. The ratio of Pt^0 changed slightly when the reaction time was extended to 48 h (Table S12, ESI†).

XPS analysis was carried out to investigate the chemical states of surface O sites (Fig. S19, ESI†). The O 1s peak at 531.7 eV was assigned to oxygen defect sites (O_{defect}), and no significant change in the O_{defect} content was observed for the 1Pt/In_2O_3 and 3Pt/In_2O_3 SACs after reaction for 1 h and 48 h. In contrast, the surface O_{defect} content increased markedly for 1Pt/In_2O_3-DI and 3Pt/In_2O_3-DI due to the over-reduction of In_2O_3 during CO_2 hydrogenation, which might inhibit the dissociation of dihydrogen.[65] Although the spent 1Pt/In_2O_3-DI and 3Pt/In_2O_3-DI have higher surface O_{defect} contents than the corresponding 1Pt/In_2O_3 and 3Pt/In_2O_3 SACs, this does not necessarily mean that they will have higher activities because XPS can probe several nanometres in depth for the samples. Synchrotron NAP-XPS measurements further confirm the change in surface oxygen defects and also provide insights into changes in the outer layers during the reaction. The *in situ* NAP-XPS data consist of (i) pretreatment at 573 K in 1.5 mTorr Ar, (ii) reduction with 10% H_2/Ar (1.5 mTorr) to simulate the initial stage of the reaction, and (iii) reaction at 573 K in 2.0 mTorr of the reaction gas mixture ($H_2/CO_2 = 3:1$). As shown in Fig. 5f, the 1Pt/In_2O_3 sample pretreated at 573 K in Ar contains more thermally induced oxygen vacancies, and exposure to the H_2/Ar atmosphere also leads to more H_2-induced vacancies. Additionally, the V_O content in the reaction atmosphere decreases slightly and remains stable, consistent with the high stability of 1Pt/In_2O_3. *In situ* SVUV-PIMS was employed to detect the gas phase products during CO_2 hydrogenation on 1Pt/In_2O_3 as shown in Fig. 5c and d. The signals of m/z at 30, 32, and 42 have ionization thresholds of 10.90, 10.85 and 11.20 eV, respectively, suggesting the presence of HCHO, CH_3OH, and HCOOH species during CO_2 hydrogenation, which supports our proposed reaction mechanism.

The H_2-TPR peak at 469 K shifts to much lower temperatures with the introduction of Pt (Fig. 5g), indicating that the active H adatoms spilling over from the Pt species to In_2O_3 can enhance the reduction of the In_2O_3 surface. Additionally, the surface reduction peaks of 1Pt/In_2O_3 and 3Pt/In_2O_3 are located at much higher temperatures than those of 1Pt/In_2O_3-DI and 3Pt/In_2O_3-DI, so bulk Pt doping makes it more difficult to create V_O sites on the In_2O_3 surface compared to surface doping. CO_2-TPD measurements show that for samples prepared by the hydrothermal method, the amount of thermally induced V_O sites increases significantly with the increasing Pt loading, while the opposite occurs for surface Pt doping (Fig. 5h and Table S13, ESI†). 1Pt/In_2O_3 has the largest total amount of V_O sites induced by thermal treatment and H_2 reduction among all samples (Fig. S20, ESI†), which is further confirmed by the greater intensity of the EPR signal (Fig. S15d, ESI†) for 1Pt/In_2O_3 than for the other samples, contributing to its higher methanol production.

Conclusions

This study demonstrates the strength of computer-aided design for constructing oxide-based catalysts for industrial reactions; the simulations predicted a bulk-doped SAC with high performance. Our DFT-based microkinetic simulations suggest that

introducing bulk Pt dopants to an In_2O_3 catalyst promotes CO_2 reactivity while maintaining CH_3OH selectivity. Our theoretical prediction facilitates the development of Pt/In_2O_3 catalysts with Pt single-atom dopants in the dominantly bulk-doped form, which show more than twice the CO_2 conversion rate and high catalytic stability while having similar CH_3OH selectivity compared with the pristine In_2O_3 catalyst. Our synthesized Pt/In_2O_3 SACs thus exhibit great potential for industrial applications in methanol synthesis from CO_2 hydrogenation, and methanol productivity reaches 1.25 g g_{cat}^{-1} h^{-1} under the reaction conditions of 5.0 MPa, 573 K and 54 000 mL g_{cat}^{-1} h^{-1}, far exceeding the current reported maximum methanol productivity, which is less than 1.0 g g_{cat}^{-1} h^{-1}.

Author contributions

S. L., D. A. D. and P. G. conceived the project. Y. W., Z. Z., Q. C., S. L., D. A. D. and P. G. designed the study, analysed the data, and wrote the paper. Y. W., Q. C., B. Q., Y. H., and Y. B. performed DFT calculations. Q. C., Y. W. and K. L. performed microkinetic simulations. Z. Z., S. D., and H. Y. prepared and characterized the samples, and performed the catalytic evaluation. J. M. and J. L. assisted with the XAS experiments. Y. L. assisted with the XPS experiments. All authors discussed the results and commented on the manuscript.

Data availability

The data supporting this article have been included as part of the ESI.†

Conflicts of interest

There are no conflicts to declare.

Acknowledgements

We thank beamline BL11B and BL02B01 at the SSRF, Shanghai, P. R. China as well as beamline BLO4B at National Synchrotron Radiation Laboratory, Hefei, P. R. China for the beam time and assistance with experiments. This work was financially supported by the National Natural Science Foundation of China (22293023, 22172189, 22172188, 22293025, U22B20136), Program of Shanghai Academic Research Leader (22XD1424100), Science and Technology Commission of Shanghai Municipality (23ZR1481700, 23YF1453400), CAS Youth Interdisciplinary Team, Chinese Academy of Sciences, Shanghai Branch (CASSHB-QNPD-2023-024), Joint Fund of the Yulin University and the Dalian National Laboratory for Clean Energy (Grant. YLU-DNL Fund 2022001), and Shell Global Solutions B. V. (CW373032, CW906044). The work at UA was supported by the U.S. Department of Energy (DOE), Office of Science, Office of Basic Energy Sciences (BES), Chemical Sciences, Geosciences, and Biosciences Division, catalysis science program (FWP 47319). D. A. D. thanks the Robert Ramsay Fund of UA for partial support.

References

1 X. Jiang, X. Nie, X. Guo, C. Song and J. G. Chen, *Chem. Rev.*, 2020, **120**, 7984–8034.
2 J. Zhong, X. Yang, Z. Wu, B. Liang, Y. Huang and T. Zhang, *Chem. Soc. Rev.*, 2020, **49**, 1385–1413.
3 M. Yang, J. Yu, A. Zimina, B. B. Sarma, L. Pandit, J. D. Grunwaldt, L. Zhang, H. Xu and J. Sun, *Angew. Chem., Int. Ed.*, 2023, **62**, e202216803.
4 M. Zabilskiy, V. L. Sushkevich, D. Palagin, M. A. Newton, F. Krumeich and J. A. van Bokhoven, *Nat. Commun.*, 2020, **11**, 2409.
5 X. Liu, J. Luo, H. Wang, L. Huang, S. Wang, S. Li, Z. Sun, F. Sun, Z. Jiang and S. Wei, *Angew. Chem., Int. Ed.*, 2022, **61**, e202202330.
6 S. Kattel, P. J. Ramírez, J. G. Chen, J. A. Rodriguez and P. Liu, *Science*, 2017, **355**, 1296–1299.
7 P. Amann, B. Klötzer, D. Degerman, N. Köpfle, T. Götsch, P. Lömker, C. Rameshan, K. Ploner, D. Bikaljevic, H.-Y. Wang, M. Soldemo, M. Shipilin, C. M. Goodwin, J. Gladh, J. Halldin Stenlid, M. Börner, C. Schlueter and A. Nilsson, *Science*, 2022, **376**, 603–608.
8 Y. Guo, X. Guo, C. Song, X. Han, H. Liu and Z. Zhao, *ChemSusChem*, 2019, **12**, 4916–4926.
9 H. Li, W. Fang, L.-X. Wang, Y. Liu, L. Liu, T. Sun, C. Liao, Y. Zhu, L. Wang and F.-S. Xiao, *The Innovation*, 2023, **4**, 100445.
10 H. Li, L. Wang, X. Gao and F.-S. Xiao, *Ind. Eng. Chem. Res.*, 2022, **61**, 10446–10454.
11 M. S. Frei, M. Capdevila-Cortada, R. García-Muelas, C. Mondelli, N. López, J. A. Stewart, D. Curulla Ferré and J. Pérez-Ramírez, *J. Catal.*, 2018, **361**, 313–321.
12 S. Dang, B. Qin, Y. Yang, H. Wang and Y. Sun, *Sci. Adv.*, 2020, **6**, eaaz2060.
13 J. Wang, G. Zhang, J. Zhu, X. Zhang and C. Song, *ACS Catal.*, 2021, **11**, 1406–1423.
14 X. Zhang, G. Zhang, W. Liu, F. Yuan, J. Wang, J. Zhu, X. Jiang, A. Zhang, F. Ding, C. Song and X. Guo, *Appl. Catal., B*, 2021, **284**, 119700.
15 D. Cai, Y. Cai, K. B. Tan and G. Zhan, *Materials*, 2023, **16**, 2803.
16 S. N. H. Dostagir, C. B. Thompson, H. Kobayashi, A. M. Karim and A. Shrotri, *Catal. Sci. Technol.*, 2021, **10**, 8196–8202.
17 X. Jia, K. Sun, J. Wang, C. Shen and C.-J. Liu, *J. Energy Chem.*, 2020, **50**, 409–415.
18 M. S. Frei, C. Mondelli, R. García-Muelas, K. S. Kley and J. Pérez-Ramírez, *Nat. Commun.*, 2019, **10**, 3377.
19 N. Rui, F. Zhang, K. Sun, Z. Liu, W. Xu, E. Stavitski, S. D. Senanayake, J. A. Rodriguez and C.-J. Liu, *ACS Catal.*, 2020, **10**, 11307–11317.
20 K. Sun, N. Rui, Z. Zhang, Z. Sun, Q. Ge and C.-J. Liu, *Green Chem.*, 2020, **22**, 5059–5066.

21 Z. Han, C. Tang, J. Wang, L. Li and C. Li, *J. Catal.*, 2021, **394**, 236–244.
22 J. Zhu, F. Cannizzaro, L. Liu, H. Zhang, N. Kosinov, I. A. W. Filot, J. Rabeah, A. Brückner and E. J. M. Hensen, *ACS Catal.*, 2021, **11**, 11371–11384.
23 F. Cannizzaro, E. J. Hensen and I. A. Filot, *ACS Catal.*, 2023, **13**, 1875–1892.
24 Z. Zhang, Y. Zhu, H. Asakura, B. Zhang, J. Zhang, M. Zhou, Y. Han, T. Tanaka, A. Wang and T. Zhang, *Nat. Commun.*, 2017, **8**, 16100.
25 Y. Ren, Y. Tang, L. Zhang, X. Liu and T. Zhang, *Nat. Commun.*, 2019, **10**, 4500.
26 B. Qiao, A. Wang, X. Yang, L. F. Allard, Z. Jiang, Y. Cui, J. Liu, J. Li and T. Zhang, *Nat. Chem.*, 2011, **3**, 634–641.
27 G. Kresse and J. Furthmüller, *Comput. Mater. Sci.*, 1996, **6**, 15–50.
28 J. Hafner and G. Kresse, in *Properties of Complex Inorganic Solids*, ed. A. Gonis, A. Meike and P. E. A. Turchi, Springer US, Boston, MA, 1997, pp. 69–82.
29 G. Kresse and J. Hafner, *Phys. Rev. B: Condens. Matter Mater. Phys.*, 1993, **47**, 558–561.
30 G. Kresse and J. Furthmüller, *Phys. Rev. B: Condens. Matter Mater. Phys.*, 1996, **54**, 11169–11186.
31 J. Wellendorff, K. T. Lundgaard, A. Mφgelhφj, V. Petzold, D. D. Landis, J. K. Nφrskov, T. Bligaard and K. W. Jacobsen, *Phys. Rev. B: Condens. Matter Mater. Phys.*, 2012, **85**, 5826–5831.
32 P. E. Blöchl, *Phys. Rev. B: Condens. Matter Mater. Phys.*, 1994, **50**, 17953–17979.
33 P. E. Blöchl, C. J. Först and J. Schimpl, *Bull. Mater. Sci.*, 2003, **26**, 33–41.
34 G. Henkelman, B. P. Uberuaga and H. Jonsson, *J. Chem. Phys.*, 2000, **113**, 9901–9904.
35 G. Henkelman and H. Jonsson, *J. Chem. Phys.*, 1999, **111**, 7010–7022.
36 K. Momma and F. Izumi, *J. Appl. Crystallogr.*, 2011, **44**, 1272–1276.
37 B. Qin and S. Li, *Phys. Chem. Chem. Phys.*, 2020, **22**, 3390–3399.
38 B. Qin, Z. Zhou and S. Li, *Appl. Surf. Sci.*, 2021, **542**, 148591.
39 P. Gao, S. Li, X. Bu, S. Dang, Z. Liu, H. Wang, L. Zhong, M. Qiu, C. Yang, J. Cai, W. Wei and Y. Sun, *Nat. Chem.*, 2017, **9**, 1019–1024.
40 P. Gao, S. Dang, S. Li, X. Bu, Z. Liu, M. Qiu, C. Yang, H. Wang, L. Zhong, Y. Han, Q. Liu, W. Wei and Y. Sun, *ACS Catal.*, 2018, **8**, 571–578.
41 B. Qin, Z. Zhou, S. Li and P. Gao, *J. CO2 Util.*, 2021, **49**, 101543.
42 J. Ye, C. Liu, D. Mei and Q. Ge, *ACS Catal.*, 2013, **3**, 1296–1306.
43 Z. Zhou, B. Qin, S. Li and Y. Sun, *Phys. Chem. Chem. Phys.*, 2021, **23**, 1888–1895.
44 A. J. Medford, C. Shi, M. J. Hoffmann, A. C. Lausche, S. R. Fitzgibbon, T. Bligaard and J. K. Nørskov, *Catal. Lett.*, 2015, **145**, 794–807.
45 C. T. Rettner, *Phys. Rev. Lett.*, 1992, **69**, 383–386.
46 T. C. Campbell, *ACS Catal.*, 2017, **7**, 2770–2779.
47 C. Stegelmann, A. Andreasen and C. T. Campbell, *J. Am. Chem. Soc.*, 2009, **131**, 8077–8082.
48 P. Sinha, A. Datar, C. Jeong, X. Deng and L. C. Lin, *J. Phys. Chem. C*, 2019, **123**, 20195–20209.
49 A. J. Medford, A. Vojvodic, J. S. Hummelshj, J. Voss and J. K. Nrskov, *J. Catal.*, 2015, **328**, 36–42.
50 X. Wang, J. Pan, H. Wei, W. Li, J. Zhao and Z. Hu, *J. Phys. Chem. C*, 2022, **126**, 1761–1769.
51 T. Liu, X. Hong and G. Liu, *ACS Catal.*, 2020, **10**, 93–102.
52 B. Hu, Y. Yin, Z. Zhong, D. Wu, G. Liu and X. Hong, *Catal. Sci. Technol.*, 2019, **9**, 2673–2681.
53 O. Martin, A. J. Martín, C. Mondelli, S. Mitchell, T. F. Segawa, R. Hauert, C. Drouilly, D. Curulla-Ferré and J. Pérez-Ramírez, *Angew. Chem., Int. Ed.*, 2016, **55**, 6261–6265.
54 M. Zabilskiy, V. L. Sushkevich, M. A. Newton, F. Krumeich, M. Nachtegaal and J. A. Bokhoven, *Angew. Chem., Int. Ed.*, 2021, **60**, 17053–17059.
55 Y. Yin, X. Bing, X. Zhou, X. Hong and G. Liu, *Appl. Catal., B*, 2018, **234**, 143–152.
56 C. Meng, G. Zhao, X. R. Shi, P. Chen, Y. Liu and Y. Lu, *Sci. Adv.*, 2021, **7**, abi6012.
57 M. M. J. Li, H. Zou, J. Zheng, T. S. Wu, T. S. Chan, Y. L. Soo, X. P. Wu, X. Q. Gong, T. Chen, K. Roy, G. Held and S. C. E. Tsang, *Angew. Chem., Int. Ed.*, 2020, **59**, 16039–16046.
58 Y. Wang, D. Wu, T. Liu, G. Liu and X. Hong, *J. Colloid Interface Sci.*, 2021, **597**, 260–268.
59 V. Dybbert, S. M. Fehr, F. Klein, A. Schaadt, A. Hoffmann, E. Frei, E. Erdem, T. Ludwig, H. Hillebrecht and I. Krossing, *Angew. Chem., Int. Ed.*, 2019, **58**, 12935–12939.
60 M. Zabilskiy, V. L. Sushkevich, M. A. Newton and J. A. Van Bokhoven, *ACS Catal.*, 2020, **10**, 14240–14244.
61 C. Wu, L. Lin, J. Liu, J. Zhang and D. Ma, *Nat. Commun.*, 2020, **11**, 5767.
62 J. Wang, G. Li, Z. Li, C. Tang, Z. Feng, H. An, H. Liu, T. Liu and C. Li, *Sci. Adv.*, 2017, **3**, e1701290.
63 F. Sha, C. Tang, S. Tang, Q. Wang, Z. Han, J. Wang and C. Li, *J. Catal.*, 2021, **404**, 383–392.
64 H. Jeong, D. Shin, B. S. Kim, J. Bae, S. Shin, C. Choe, J. W. Han and H. Lee, *Angew. Chem., Int. Ed.*, 2020, **59**, 20691–20696.
65 C. Shen, K. Sun, Z. Zhang, N. Rui, X. Jia, D. Mei and C.-J. Liu, *ACS Catal.*, 2021, **11**, 4036–4046.